

A mechanistic study of impurity segregation at silicon grain boundaries

Peter Käshammer and Talid Sinno^{a)}

Department of Chemical and Biomolecular Engineering, University of Pennsylvania, Philadelphia, Pennsylvania 19104, USA

(Received 27 June 2015; accepted 11 August 2015; published online 1 September 2015)

The segregation behavior of carbon and oxygen atoms at various silicon grain boundaries was studied using a combination of atomistic simulation and analytical modeling. First, quasi-lattice Grand Canonical Monte Carlo simulations were used to compute segregation isotherms as a function of grain boundary type, impurity atom loading level, and temperature. Next, the atomistic results were employed to regress different analytical segregation models and extract thermodynamic and structural properties. The multilayer Brunauer–Emmett–Teller (BET) isotherm was found to quantitatively capture all the simulation conditions probed in this work, while simpler, single layer models such as the Langmuir–McLean model did not. Some of the BET parameters, namely, the binding free energy of the first adsorption layer and the impurity holding capacity of each layer, were tested for correlation with various measures of grain boundary structure and/or mechanical properties. It was found that certain measures of the atomistic stress distribution correlate strongly with the first-layer binding free energy for substitutional carbon atoms, while common grain boundary identifiers such as sigma value and energy density are not useful in this regard. Preliminary analysis of the more complex case of interstitial oxygen segregation showed that similar measures based on atomistic stress also may be useful here, but more systematic correlative studies are needed to develop a comprehensive picture. © 2015 AIP Publishing LLC.

[<http://dx.doi.org/10.1063/1.4929637>]

I. INTRODUCTION

Multicrystalline silicon (mc-Si) based solar cells, most commonly grown by the directional solidification (DS) method, now account for over 60% of the global photovoltaic (PV) market. Mc-Si, in contrast to the single-crystal material grown by the Czochralski technique, is characterized by the presence of grain boundaries and dislocations. These extended defects are frequently intrinsically electrically active, and also act as preferential segregation sites for various electrically active impurity species introduced either through the silicon feedstock or by components in the crystal growth assembly. As a result, mc-Si solar cells are somewhat less efficient than those fabricated on single-crystal Si, and perhaps of more concern, can exhibit a much larger variance of efficiencies whose origin has been linked to the microscopic details of the grain boundary and dislocation distributions.

Consequently, engineering of the grain boundary and dislocation distribution during mc-Si solidification has received much attention. Unfortunately, dislocation density, grain size and orientation, and grain boundary distribution are closely linked, making their individual impacts on the ultimate quality of the material difficult to isolate.^{1–3} Dislocation multiplication is known to be driven by thermal stress generated during solidification and also by expansion stresses against the crucible walls. Dislocations are electrically active and also strongly bind metallic and other impurity atoms and therefore are always undesirable. Grain

boundaries are also generally electrically active and may be strong attractors for harmful impurities; a notable exception is the $\Sigma\{111\}$ twin.⁴ Thus, the classical approach for mc-Si optimization was to minimize grain boundary density by maximizing grain size or to somehow control grain boundary distribution.^{5–7} More recently, the discovery that certain types of grain boundaries, particularly high-energy, incoherent ones, blunt the multiplication rate of dislocations has led to a fundamentally different approach for mc-Si optimization in which grain size is tailored to minimize dislocation density during the early phase of the solidification process.^{3,8} This new strategy has led to rapid improvements in mc-Si efficiency in a short period of time.

Nonetheless, contaminant segregation to grain boundaries remains an important limitation to mc-Si quality and is still quite poorly studied in silicon. In particular, the segregation of large numbers of mobile atomic species at grain boundaries is likely to play an important role in the formation of highly detrimental precipitates such as SiO_2 , SiC, Si_3N_4 , and metal silicides.^{4,9–16} Such precipitates are harmful because they alter the electrical properties of the mc-Si material by acting as charge carrier recombination centers and electrical shunts. They can also impact the mechanical properties of the material; for example, SiC precipitates hinder the wafer cutting process due to their hardness.

Most experimental studies that relate solute segregation tendency to grain boundary structure have been performed in metallic systems.¹⁷ A systematic correlation of segregation strength is commonly performed with macroscopic grain boundary parameters, e.g., misorientation angle,^{18–22} grain boundary plane,²³ or Σ -value.^{24–26} One general conclusion

^{a)}Author to whom correspondence should be addressed. Electronic mail: talid@seas.upenn.edu

of these studies is that segregation strength increases with misorientation of both tilt^{21,22} and twist²⁰ grain boundaries. A differentiation between small angle and large angle boundaries is also necessary, the former tend to attract more strongly the segregating atomic species.^{17,20} Nonetheless, some contradictory and inconclusive correlations are also obtained.¹⁷ In particular, the occurrence of “special” grain boundary types, e.g., small Σ -value grain boundaries, proved that segregation tendencies do not just simply align with the relative change of a single macroscopic parameter.^{17,19} Rather, a detailed inspection of the microstructure of a grain boundary is necessary to understand its segregation tendency.

By contrast, impurity atom segregation on grain boundaries in mc-Si has not been explored extensively, and the few reported studies focus on metal impurities (mainly Fe) due to their detectability by X-ray based techniques.²⁷ Also here, correlations to grain boundary structure were only performed with respect to macroscopic grain boundary parameters. For example, Buonassisi *et al.*²⁸ found that metal segregation to twin grain boundaries increases with twinning order. Grain boundaries that do not belong to the $\Sigma 3$ – $\Sigma 9$ – $\Sigma 27$ twinning network showed slightly more pronounced metal decoration. In another comprehensive study, Chen *et al.*²⁹ compared the iron content at three different $\Sigma 3$ twin boundaries in mc-Si. They found that both the grain boundaries with $\{110\}$ and $\{112\}$ grain boundary planes accumulate iron, while the $\Sigma 3\{111\}$ grain boundary remains undecorated.

Quantitative, experimental grain boundary segregation studies in mc-Si that have been performed on non-metallic impurities have been restricted to dopant elements, i.e., boron, phosphorus, and arsenic. In these studies, the segregation extent was inferred by measuring charge carrier density and electrical resistivity,^{30–34} and the segregation extent was correlated to temperature and bulk dopant concentration, but not with grain boundary structure. Finally, the segregation of common light impurities, such as carbon, oxygen, or nitrogen, has only recently been experimentally correlated to grain boundary structure³⁵ and little data exists in the literature. The primary reason for the dearth of such studies is the challenge of detecting these atomic species with high spatial resolution.

Bearing these factors in mind, computational approaches provide an excellent opportunity to complement existing experimental findings. In contrast to the large amount of computational segregation studies for metal oxides,^{36,37} and bimetallic alloys,^{17,38–43} to our knowledge, only two studies have been published for mc-Si. In Ref. 44, two single core sites of a $\Sigma 3$ – $\Sigma 3$ – $\Sigma 9$ grain boundary triple-junction were substituted with single impurity atoms such as boron, carbon, and nitrogen and binding energies were interpreted in terms of elasticity arguments. More recently, we considered the binding energies of single carbon and germanium atoms on various sites in twin grain boundaries using several different interaction potential models.⁴⁵

While the considerations of single atom substitutions provides some insight into grain boundary-impurity atom segregation, single-atom/single-site studies do not provide insight into collective, multi-atom interactions which are

likely to represent experimental conditions. In this paper, we employ simulations that allow for the consideration of populations of segregating impurity atoms, namely, carbon and oxygen. In particular, we develop a Grand Canonical Monte Carlo (GCMC) simulation approach to study segregation at 8 structurally diverse grain boundaries in mc-Si. Impurity segregation is analyzed as a function of impurity type, bulk impurity concentration, temperature, as well as grain boundary structure. In order to assist with this task, the segregation behavior for each grain boundary is described in using classical analytical segregation models that are fit to the simulation data.

The remainder of the paper is organized as follows. The SGMC method first is described in Section II. The SGMC simulation results are presented in Section III, while the analytical segregation models are discussed in Section IV. In Section V, we investigate the relationship between segregation model parameters and various measures of grain boundary structure. Some preliminary investigations of the temperature dependence of grain boundary segregation are described in Section VI. Finally, conclusions are provided in Section VII.

II. METHODS

A. Choice of interatomic potential model

There are numerous empirical potential models for pure Si that describe various properties for varying degrees of fidelity. However, potentials that model the interactions between Si and light elements such as oxygen^{46–48} and carbon^{49–51} are relatively limited. Here, we employ the Tersoff potential framework, which has been parametrized to account for Si-O and Si-C interactions. Specifically, we use two different parameterizations of the potential: (1) the Erhart-Albe (EA) potential⁵¹ for Si-C and (2) the Munetoh (MT) potential⁴⁶ for Si-O interactions.

The choice of the EA potential is motivated by its comparably good description of intrinsic point defect properties in Si,⁵¹ and its successful application to grain boundaries.^{45,52} A known weakness of the EA potential (and most parametrizations of the Tersoff model) is the significant overestimate of the silicon melting point (~ 2450 K versus 1685 K), but numerous prior investigations show that using a reduced temperature, T/T_m , allows for a reasonably direct comparison to experimental conditions and results from other potentials. The MT potential for Si-O has been validated in previous studies that demonstrate its ability to describe various bulk amorphous SiO₂ properties, including a good description of Si-O-Si bond angles for single oxygen interstitials in the silicon lattice.^{46,53,54} That said the oxygen segregation results presented later in the paper should be considered to be somewhat speculative given the fact that the MT potential represents a highly simplified view of Si-O interactions.

B. Bicrystal simulation domain construction

The grain boundary segregation simulations in this work were conducted in eight different bicrystal simulation

TABLE I. Structural comparison of the grain boundaries modeled in this work. An explanation of the structural unit types within a GB can be found in Ref. 55, GB energies, γ , are based on the EA potential.⁵¹

CSL	GB plane	Rotation axis	Misorientation angle	Inclination angle	Structural units	γ (J/m ²)
$\Sigma 3$	{111}	tilt $\langle 110 \rangle$	70.53	0.00	{TT}	0.00
$\Sigma 3$	{110}/{114}	tilt $\langle 110 \rangle$	70.53	35.26	{TTTTL}	0.54
$\Sigma 3$	{112}	tilt $\langle 110 \rangle$	70.53	90.00	{MDT}	0.83
$\Sigma 9$	{221}	tilt $\langle 110 \rangle$	38.94	0.00	{M ⁺ M ⁻ }	0.55
$\Sigma 27$	{552}	tilt $\langle 110 \rangle$	31.50	0.00	{L ⁺ L ⁻ CL ⁻ L ⁺ C}	0.66
$\Sigma 5$	{310}	tilt $\langle 001 \rangle$	53.13	0.00	{AA}	0.83
$\Sigma 25$	{430}	tilt $\langle 001 \rangle$	16.26	0.00	{APPPPP}	0.85
$\Sigma 5$	{001}	twist $\langle 001 \rangle$	53.13	0.00	“Amorphous”	1.39

domains, each subject to periodic boundary conditions in all three dimensions. The total system sizes ranged from 1600 to 3456 atoms. Simulation cell construction was guided by reported grain boundary structures from *ab-initio* data, MD-simulations, as well as experimental images.^{55–63} The simulation cell construction is based on a combination of (1) finite temperature molecular dynamics simulations, (2) conjugate gradient (CG) energy minimization, and (3) atom deletions and insertions in the grain boundary region. Step (1) was used to anneal two differently oriented grains in a specified grain boundary plane. The high temperature anneal was employed to allow lateral shift between the grains when forming the grain boundary. Steps (2) and (3) were then conducted to relax the grain boundary. Steps (1) and (2) were performed with the LAMMPS software⁶⁴ in the NST-ensemble, i.e., the number of particles, N , the temperature, T , and the applied stress in all three dimensions, S_{xx} , S_{yy} , S_{zz} , was held constant during the simulation. All GB structures were visualized with the OVITO software⁶⁵ and checked for consistency with the literature. More details of the grain boundary construction and relaxation procedure are provided in Ref. 45.

All final simulation domains contained two grain boundaries of the same type, each of which is characterized by its Σ -value and the grain boundary plane. Note that a grain boundary structure is only uniquely identified by also considering its precise microstructure, which is denoted by grain boundary “structural units”;⁵⁵ grain boundary microstructure varies according to the lateral shift and the surface truncations of the adjoining grains. All grain boundaries considered in this work were built in the lowest-energy microstructure. A summary of the details for each grain boundary is provided in Table I and their configurations are shown in Figure 1.

The pool of grain boundary structures in Figure 1 was chosen to reflect grain boundary types that are structurally diverse and frequently detected in mc-Si. The most common grain boundary is the coherent first order twin grain boundary, $\Sigma 3\{111\}$, which has no significant formation energy. In terms of abundance, it is followed by other $\Sigma 3$ -grain boundaries as well as higher-order twin boundaries, i.e., $\Sigma 9\{221\}$ and $\Sigma 27\{552\}$. Higher-order twin grain boundaries are formed by the “reaction” of lower-order twins.⁶⁶ Collectively, these grain boundaries represent more than 50% of all grain boundaries found in “traditional” mc-Si grown without specifically

engineering the material to include high concentrations of incoherent grains.^{67,68} Three different $\langle 110 \rangle$ -tilt $\Sigma 3$ grain boundaries with different planes were modeled because studies^{29,56} have indicated that both the Σ -value and the grain boundary plane influence the grain boundary energy, structure, and segregation strength. All three high-coincidence grain boundaries are characterized by a misorientation angle of 70.53° but differ in inclination angle. The resulting $\Sigma 3$

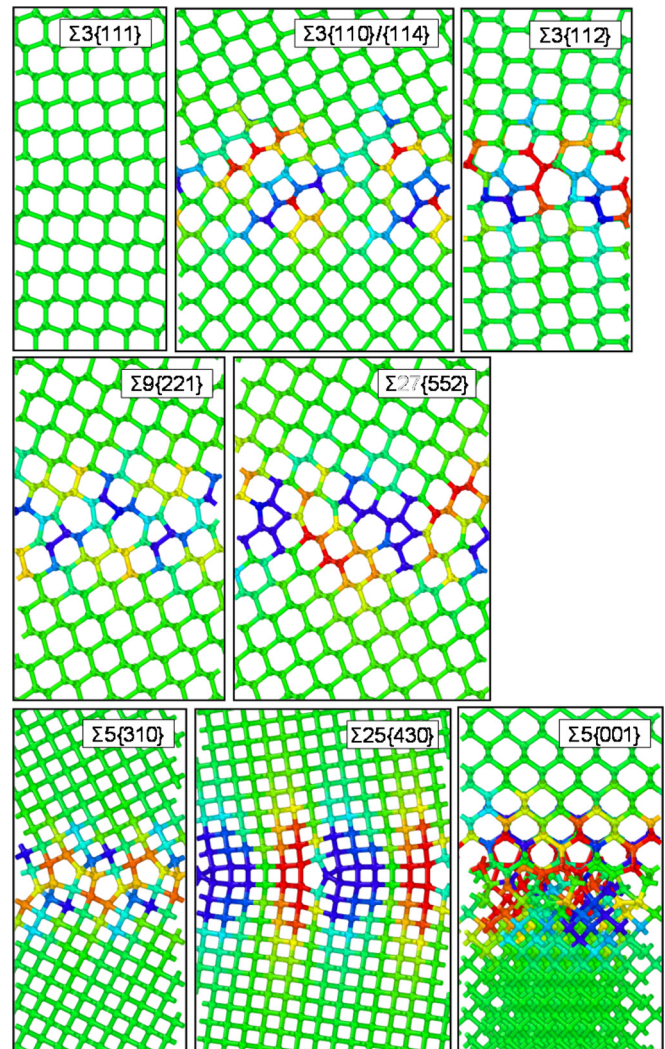


FIG. 1. Cross sections of the 8 grain boundaries considered in this work. The color coding represents the atomic hydrostatic pressure distribution: red ≤ -3 GPa (tension); blue $\geq +3$ GPa (compression).

grain boundaries are symmetric in the case of the $\Sigma 3\{111\}$ grain boundary (coherent) and the $\Sigma 3\{112\}$ grain boundary (incoherent) and asymmetric in the case of the $\Sigma 3\{110\}/\{114\}$ grain boundary.

We also consider two grain boundaries that are tilted around a $\langle 001 \rangle$ -axis by 53.13° and 16.26° , i.e., the $\Sigma 5\{310\}$ and the $\Sigma 25\{430\}$ grain boundaries, respectively. These grain boundaries can be considered as arrays of edge dislocations, where the distance between the dislocation cores decreases with increasing tilt angle. Two different kinds of dislocation arrays are chosen in order to study the influence of edge dislocation separation on impurity segregation at grain boundaries. Finally, a high energy twist grain boundary, $\Sigma 5\{001\}$, was constructed by twisting the adjoining grains around a $\langle 001 \rangle$ axis by 53.13° . Here, the rotation axis lies normal to the grain boundary plane, in contrast to the previous cases where the axis lies in the grain boundary plane. While twist grain boundaries around a $\langle 110 \rangle$ can be considered as arrays of screw dislocations, a twist around a $\langle 001 \rangle$ axis was chosen since it causes the grain boundary structure to be highly disordered. The origin of the disorder in the grain boundary is the comparably large lattice spacing between $\{001\}$ planes. This causes the grain boundary to contain several mis-coordinated bonds, i.e., consisting of 3- and 5-fold coordinated Si atoms. This grain boundary is intended to be representative of the high-energy random grain boundaries engineered in so-called high-performance mc-Si.

For all cases, the grain boundary “region” was defined to include all atomic sites within 7.5 \AA from the grain boundary centerline (15 \AA total width). Although this definition is somewhat arbitrary, it was found that the results (see later) depended only weakly on the precise definition of the grain boundary region. Other criteria based on atomic energies or stress led to similar results.

C. Simulation of impurity segregation to grain boundaries with GCMC

Monte Carlo simulations in the grand canonical statistical ensemble were performed under constant volume, V , temperature, T , chemical potential, μ , while the number of impurity atoms within the system, N , fluctuates around a set-point that is controlled by the chemical potential. Strictly speaking, the carbon simulations represent a semi-grand statistical ensemble because the total number of particles in the system is constant and only the atom ratio of C-to-Si changes.

A quasi-lattice framework for the GCMC simulations was employed in which the overall domain consists of well-defined sites,^{38,69} but where elastic relaxation is accommodated. Three types of moves were defined for both the carbon and oxygen cases. For substitutional carbon these are (1) switching of atomic positions of a carbon and silicon atom, (2) insertion of a new carbon atom by replacing an existing silicon atom, and (3) deletion of an existing carbon atom by replacing it with a new silicon atom. In the case of oxygen, which exists as an interstitial that occupies the center of a Si-Si-bond with an equilibrium angle of $130^\circ \leq \alpha(\text{Si} - \text{O} - \text{Si}) \leq 180^\circ$,⁵⁴ steps

(1)–(3) are essentially unchanged. For both cases, all atomic positions are randomly picked for each move. The lattice relaxation after each move is conducted using a conjugate-gradient (CG) energy minimization routine (see below). The energies, $E_a(N)$ and $E_b(N)$, of the system before (denoted by the subscript a) and after (subscript b) a move were used to accept or reject a move according to the Metropolis criterion,⁷⁰ i.e.,

$$\text{acc}(a \rightarrow b) = \min(1, \exp\{ -[E_b(N) - E_a(N)]/k_B T \}), \quad (1)$$

where k_B is the Boltzmann constant. Insertion and deletion moves of impurity atoms were accepted according to

$$\text{acc}(a \rightarrow b) = \min\left(1, \frac{V}{\Lambda^3(N+1)} \exp\{ [\mu - E_b(N+1) + E_a(N)]/k_B T \} \right), \quad (2)$$

and

$$\text{acc}(a \rightarrow b) = \min\left(1, \frac{\Lambda^3 N}{V} \exp\{ -[\mu + E_b(N-1) - E_a(N)]/k_B T \} \right), \quad (3)$$

respectively. Here, Λ is the thermal de-Broglie wavelength, $\Lambda = h/\sqrt{2\pi m k_B T}$, where h is Planck's constant and m is the mass of an impurity atom. The temperature was set to either $0.6 T_m$ or $0.8 T_m$ for all simulations described in this work.

A simulation was initialized by first statically relaxing, at zero applied stress, the impurity-free simulation domain. Next, the chemical potential was initially set to produce a low bulk impurity atom fraction, X_{BULK} . A GCMC simulation consisted of repeated blocks of 10 insertion, 10 removal, and 20 switch moves performed in a random sequence. Local CG energy minimization was performed after each move, where only atoms within a sphere of radius 10.5 \AA around affected atoms were relaxed. Following each block of 40 GCMC moves, an additional global energy minimization was performed on the entire simulation domain. Convergence of the impurity segregation extent was monitored using the running average evolution of X_{BULK} and X_{GB} (the impurity fraction in the grain boundary region). The number of GCMC blocks required to reach equilibrium was found to depend on the impurity concentration, the impurity type, and the grain boundary structure. Once sufficient data for a given chemical potential were obtained, the chemical potential was increased—thereby increasing the impurity concentration—and the run continued. Several runs with different random number seed initializations were performed at each chemical potential to reduce statistical uncertainty.

III. SEGREGATION ISOTHERMS FROM GCMC SIMULATIONS

Shown in Figure 2 is a summary of all segregation isotherms for carbon [panels (a) and (c)] and oxygen [panels (b) and (d)], computed at $0.6 T_m$. Panels (a) and (b) show linear

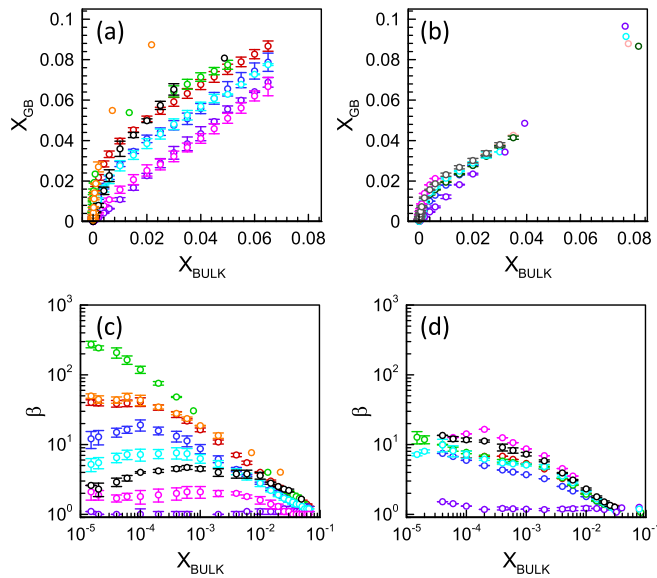


FIG. 2. Segregation isotherms for carbon [(a) and (c)] and oxygen [(b) and (d)] at $0.6T_m$. (a) and (b) Impurity fractions in the grain boundary as a function of bulk impurity fraction, (c) and (d) segregation coefficient, β , as a function of bulk impurity fraction. Each color represents a different grain boundary type: green— $\Sigma 25\{430\}$; orange— $\Sigma 5\{001\}$; red— $\Sigma 27\{552\}$; blue— $\Sigma 3\{110\}/\{114\}$; cyan— $\Sigma 9\{221\}$; black— $\Sigma 5\{310\}$; pink— $\Sigma 3\{112\}$; purple— $\Sigma 3\{111\}$. The color coding in this figure is used throughout the paper.

plots of X_{GB} vs. X_{BULK} , while panels (c) and (d) are log-log plots of the grain boundary segregation coefficient, defined as

$$\beta = \frac{X_{GB}}{X_{BULK}}, \quad (4)$$

as a function of X_{BULK} . Error bars are obtained from averaging GCMC data from different random number seeds. The impurity fractions/segregation coefficients shown in Figure 2 correspond to a single impurity atom at the low end to about 150–200 impurity atoms at the maximum impurity concentration. Note that no segregation isotherm is shown for oxygen at the $\Sigma 5\{001\}$ grain boundary because the interstitial oxygen placement algorithm (Section II C) is only applicable to four-fold coordinated silicon atoms.

Generally, segregation strength depends on (1) bulk impurity concentration, (2) grain boundary structure, and (3) impurity type. In most cases, the segregation coefficient increases monotonically with impurity concentration because the most strongly binding sites become occupied first and weaker sites only become occupied as impurity loading is increased. A notable exception to this general trend is apparent for the $\Sigma 3\{111\}$ grain boundary (purple) for both impurity types, which exhibits an approximately constant segregation coefficient of $\beta \sim 1$ over the entire range of X_{BULK} . In other words, the coherent first order twin grain boundary has no binding sites for either impurity type.^{4,28,29,45}

Several other grain boundaries also deviate from the general trend of decreasing average segregation strength with loading, including the $\Sigma 5\{310\}$ grain boundary (black), the $\Sigma 9\{221\}$ grain boundary (cyan), and the $\Sigma 3\{110\}/\{114\}$ grain boundary (blue) for carbon. In these cases, as impurity

loading decreases, β first increases then decreases after reaching a maximum value at intermediate loading. This behavior could be explained by some type of cooperative effect between impurity atoms and appears to exist for grain boundaries in which very strong binding sites are absent (see Section II B). More generally, the carbon segregation isotherms appear to span a wider range of values ($1 \leq \beta \leq 300$) than the corresponding ones for oxygen ($1 \leq \beta \leq 20$). These differences will be explored in more detail in Sections IV and V.

IV. ANALYTICAL MODELING OF IMPURITY SEGREGATION

Direct interpretation of the segregation isotherms in terms of grain boundary structure is difficult because both the segregation isotherms and the microstructural details of grain boundaries represent high-dimensional information. To facilitate this task, one must generate low-dimensional representations of the segregation behavior and the grain boundary structure. Here, we focus on the former by fitting analytical segregation models to the GCMC data in order to extract a small set of physically meaningful parameters that may be correlated with grain boundary structural descriptors.

The development and application of analytical models for species segregation on grain boundaries are well established in the literature, particularly, for metallic systems; the reader is referred to Refs. 17, 71, and 72 for comprehensive reviews. To provide context for the particular choices applied in the present work, a brief overview is provided here of the various types of segregation models. Models may be classified according to (1) how they group different types of grain boundary sites and (2) how impurity atom interactions are modeled in the description of the segregation thermodynamics. In the context of site grouping, for example, a segregation model may assume that all sites are equivalent (a monolayer model⁷³), group similar sites together into a few distinct categories (a multilayer model⁷⁴), or treat each grain boundary site with individual thermodynamic parameters (a site-by-site model⁷⁵).

The simplest segregation model, the Langmuir-McLean isotherm (LANG),⁷⁶ employs a single, constant segregation free energy, ΔG_1 , and monolayer capacity, X_{GB}^{ml} , and relates the grain boundary impurity fraction to the bulk impurity fraction according to

$$\frac{X_{GB}}{X_{GB}^{ml} - X_{GB}} = \frac{X_{BULK}}{1 - X_{BULK}} \exp(-\Delta G_1/k_B T). \quad (5)$$

Implicit in Eq. (5) is the assumption that the solid solution comprised of impurity atoms and silicon host sites is a regular solution. Numerous monolayer models subsequently were introduced to incorporate refinements to the segregation free energy description. For example, Fowler and Guggenheim⁷⁷ added an loading-dependent energetic interaction between solute atoms in the grain boundary. Schuh *et al.*^{71,78} included atomic interactions for solute-solute, solute-solvent, and solvent-solvent atom pairs in the grain boundary and bulk regions. Wynblatt and Ku^{72,79} include several energetic and

entropic contributions related to elastic effects, solute and solvent atom interactions, and grain boundary energy.

As mentioned above, another way of increasing the degrees-of-freedom in a segregation model is to invoke a multilayer description in which grain boundary sites are grouped into multiple, distinct categories. For example, Wynblatt *et al.*^{72,80,81} described a model in which sites on individual atomic planes on either side of a grain boundary are grouped into distinct layers. By introducing parameters to account for the bonding network across grain boundary planes and an enthalpic segregation contribution on each plane, the segregation behavior of a grain boundary was related to the grain boundary plane and twist angle, although the required parameters are difficult to measure. Seah and Hondros^{82,83} employed a parametrically simpler approach based on the Brunauer–Emmett–Teller (BET) isotherm with two free energy parameters, ΔG_1 and ΔG_L , to describe segregation an innermost monolayer, and an infinite number of identical “outer” layers, respectively. Note that these “layers” do not explicitly represent well-defined spatial regions as in the Wynblatt model. The latter free energy, ΔG_L , may be interpreted as condensation free energy that represents the formation of a condensed solute phase on an already-formed nucleus provided by the first monolayer. In the standard BET model, impurity segregation on a grain boundary is given by

$$\frac{X_{GB}^{ml} X_{BULK}}{X_{GB} X_{BULK}^{sol} - X_{BULK}} = \frac{1}{K} + \frac{K-1}{K} \frac{X_{BULK}}{X_{BULK}^{sol}}, \quad (6)$$

where $K \equiv \exp [-(\Delta G_1 - \Delta G_L)/k_B T]$ and $X_{BULK}^{sol} \equiv \exp [-\Delta G_L/k_B T]$ is the bulk solubility of the impurity.

The standard BET model in Eq. (6) corresponds to infinite segregation capacity, with an unbounded number of segregation monolayers. An alternative version of the BET model restricts the segregation capacity with a finite number, n , of monolayers according to

$$X_{GB} = \frac{X_{GB}^{ml} K \alpha}{(1 - \alpha)} \left[\frac{1 - (n+1)\alpha^n + n\alpha^{n+1}}{1 + (K-1)\alpha - K\alpha^{n+1}} \right], \quad (7)$$

where $\alpha \equiv X_{BULK}/X_{BULK}^{sol}$.

In the following analysis, we employ both the LANG [Eq. (5)] and finite-capacity BET [Eq. (7)] models to describe carbon and oxygen segregation to grain boundaries. The finite-capacity BET model is used to account for the fact that the GCMC simulation regions associated with grain boundaries are finite in the normal direction (7.5 Å on either side of the grain boundary). Note that the parameter n does not necessarily correspond to a specific number of atomic layers for each case. Vibrational entropy contributions, $S_{vib,1}$ and $S_{vib,L}$, may be implicitly included in the BET model via the segregation free energies, ΔG_1 and ΔG_L , respectively.

Regression of the 4-parameter (X_{BULK}^{sol} , X_{GB}^{ml} , K , and n) finite-capacity BET model to the GCMC data shown in Section III was performed using a 2-step, 4-dimensional parametric scan for each temperature and impurity type. First, a single value of X_{BULK}^{sol} was assumed for all grain boundaries because this parameter does not depend on grain

boundary structure. Then, for each grain boundary, the corresponding optimal values of X_{GB}^{ml} , K , and n were found using 3-dimensional parametric scans. The process was repeated using different values of X_{BULK}^{sol} . The optimum 4-parameter set was determined as the one that minimized the global objective function

$$OF = \frac{1}{8} \sum_{i=1}^8 \sqrt{\frac{\sum_j [X_{GB}^{MOD} - X_{GB}^{MD}]^2}{\sum_j [X_{GB}^{MOD}]^2}}, \quad (8)$$

where the inner j -sums are taken over the number of comparison points along each segregation isotherm, the outer i -sum runs over all 8 grain boundaries, and X_{GB}^{MOD} and X_{GB}^{MD} represent the equilibrium grain boundary impurity fractions obtained from the analytical model and the GCMC simulations, respectively.

The objective function in Eq. (8) is shown in Figure 3 as function of X_{BULK}^{sol} at optimal values of the remaining 3 parameters (summed over all grain boundaries), for the case of carbon segregation at $0.6 T_m$; the objective function exhibits a single, well-defined global minimum at $X_{BULK}^{sol} = 0.08$. A summary of the best-fit parameters is provided in Table II for all grain boundaries, impurity species and temperatures. For most grain boundaries, the optimum number of layers is finite and contained in the interval $4 \leq n \leq 7$, although some cases do not show a well-defined objective function minimum along this parameter, particularly the cases in which oxygen segregation is considered; these cases are denoted by $n > 7$.

The finite-capacity BET (parameters given in Table II) and LANG (parameters not shown) model fits for carbon segregation at $0.6 T_m$ are shown alongside the GCMC data in Figure 4 for several grain boundaries. In all cases, the BET model is able to capture very precisely the details of the isotherms, whereas the LANG model fails qualitatively in several cases and is only able to capture the cases in which the segregation is weak or non-existent, e.g., the $\Sigma 3\{111\}$ grain boundary. The robustness of the finite-capacity BET was probed further by comparing the best possible objective function values for the carbon segregation isotherm at the $\Sigma 27\{552\}$ grain boundary at $0.6 T_m$ for several different analytical models; the results are shown in Table III. Again, the finite-capacity BET produces the best fit to the Monte Carlo data, although this model does contain the largest number (4) of fitting parameters. On the other hand, the superiority of

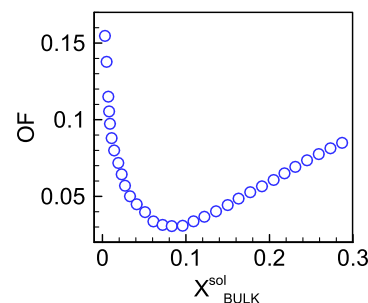


FIG. 3. Dependence of global objective function, Eq. (8), on X_{BULK}^{sol} for carbon segregation at $0.6 T_m$.

TABLE II. Finite-capacity BET regression parameters for carbon and oxygen, each at $0.6T_m$ and $0.8T_m$, based on the EA⁵¹ and the MT⁴⁶ potentials, respectively.

GB type	Impurity	T (T_m)	ΔG_1 (eV)	ΔG_L (eV)	X_{GB}^{ml}	n
$\Sigma 27 \{552\}$	C	0.6	-0.84	-0.32	0.04	4
$\Sigma 3 \{110\}/\{114\}$	C	0.6	-0.71	-0.32	0.035	4
$\Sigma 3 \{111\}$	C	0.6	-0.45	-0.32	0.036	4
$\Sigma 25 \{430\}$	C	0.6	-0.99	-0.32	0.046	3
$\Sigma 9 \{221\}$	C	0.6	-0.68	-0.32	0.035	4
$\Sigma 3 \{112\}$	C	0.6	-0.62	-0.32	0.024	6
$\Sigma 5 \{310\}$	C	0.6	-0.55	-0.32	0.069	2
$\Sigma 5 \{001\}$	C	0.6	-0.76	-0.32	0.069	>7
$\Sigma 27 \{552\}$	C	0.8	-0.98	-0.42	0.038	5
$\Sigma 9 \{221\}$	C	0.8	-0.81	-0.42	0.036	5
$\Sigma 3 \{112\}$	C	0.8	-0.68	-0.42	0.029	6
$\Sigma 27 \{552\}$	O	0.6	-0.63	-0.29	0.032	7
$\Sigma 3 \{110\}/\{114\}$	O	0.6	-0.59	-0.29	0.033	>7
$\Sigma 3 \{111\}$	O	0.6	-0.42	-0.29	0.048	5
$\Sigma 25 \{430\}$	O	0.6	-0.65	-0.29	0.03	7
$\Sigma 9 \{221\}$	O	0.6	-0.70	-0.29	0.028	>7
$\Sigma 3 \{112\}$	O	0.6	-0.82	-0.29	0.025	>7
$\Sigma 5 \{310\}$	O	0.6	-0.74	-0.29	0.028	>7
$\Sigma 27 \{552\}$	O	0.8	-0.80	-0.38	0.035	6
$\Sigma 9 \{221\}$	O	0.8	-0.78	-0.38	0.036	7

the unbounded (infinite number of monolayers) BET relative to the Fowler and Guggenheim model,⁷⁷ which is a monolayer model that includes an additional parameter to

TABLE III. Comparison of fitting quality for various segregation models applied to carbon segregation at the $\Sigma 27\{552\}$ grain boundary at $0.6T_m$.

Model	Parameter	OF
BET multilayer finite ^{74,82,83}	4	0.027
BET multilayer infinite ^{82,83}	3	0.044
Truncated BET monolayer ^{82,83}	3	0.158
Fowler monolayer ⁷⁷	3	0.183
LANG monolayer ⁷⁶	2	0.216

describe solute atom interactions, provides evidence that a multilayer description is necessary because both are 3-parameter models. At least for the cases considered here, the multilayer flexibility appears to be sufficient to fully describe carbon segregation without the need to include solute atom interactions.

Finally, carbon and oxygen segregation behavior at $0.6T_m$ is compared in Figure 5 for a subset of the grain boundaries. Here, the GCMC data (symbols) are fit with finite-capacity BET model (lines—parameters provided in Table II). Over the solute concentrations considered with the GCMC simulations, the segregation of carbon is stronger than that of oxygen at all 3 grain boundaries. Again, it is important to note that the assumption placed on the configuration of oxygen interstitial atoms becomes more uncertain as the concentration of oxygen atoms increases because the local relaxation procedure employed in Section II C would

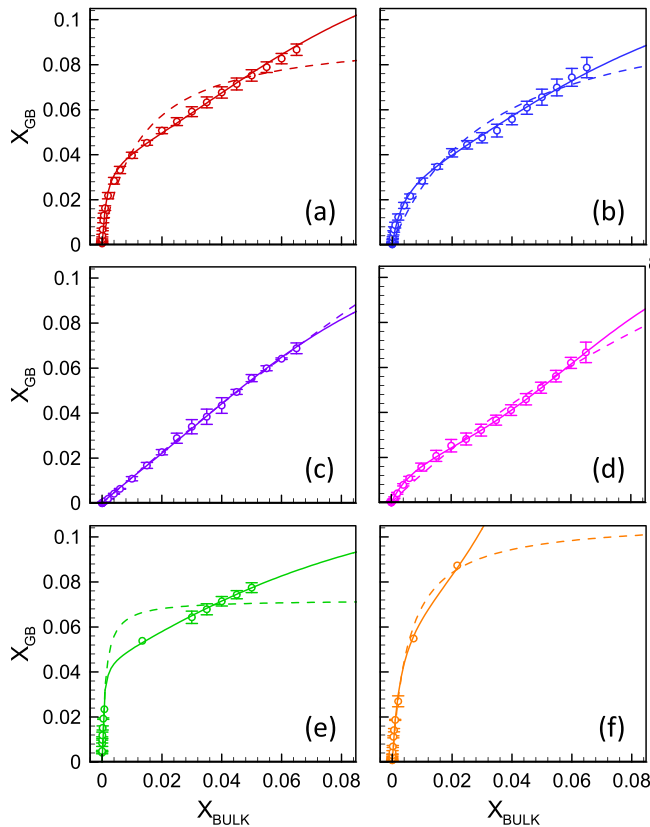


FIG. 4. Comparison of analytical models for carbon segregation at different grain boundaries at $0.6T_m$. Symbols are computational data, full/dashed lines are best fits of BET/LANG models, respectively. (a) $\Sigma 27\{552\}$; (b) $\Sigma 3\{110\}/\{114\}$; (c) $\Sigma 3\{111\}$; (d) $\Sigma 3\{112\}$; (e) $\Sigma 25\{430\}$; (f) $\Sigma 5\{001\}$.

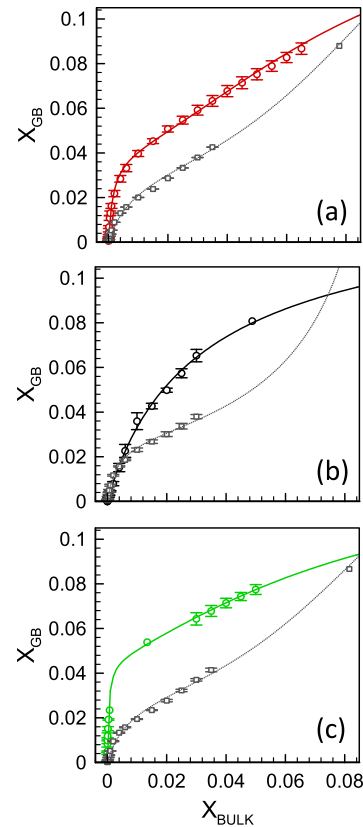


FIG. 5. Comparison of carbon (colored) and oxygen (grey) segregation at different grain boundaries at $0.6T_m$. Symbols represent GCMC data, lines represent best-fits for the finite-capacity BET model: (a) $\Sigma 27\{552\}$; (b) $\Sigma 5\{310\}$; (c) $\Sigma 25\{430\}$.

not be able to capture, for example, the formation of a new oxide phase.

V. CORRELATION OF BET MODEL PARAMETERS TO GRAIN BOUNDARY STRUCTURE

The fitting of a simple 4-parameter model such as the finite-capacity BET isotherm to the GCMC segregation data effectively remaps the segregation data onto a 4-dimensional space whose axes correspond to physically meaningful quantities. On the other hand, making a connection between these parameters and grain boundary structure remains difficult until a similar transformation is applied to the latter. As mentioned earlier, grain boundary structure is defined by a combination of “macroscopic” parameters such as the grain boundary orientation, and microscopic information that describes the details of atomic rearrangements. Unfortunately, systematically projecting the grain boundary structure onto a low-dimensional space comprised of physically intuitive variables is not possible. Instead, we consider a small set of obvious coarse structural and non-structural measures in order to assess their relative strengths. Shown in Figure 6 are plots showing the correlation between various measures of grain boundary configuration and the BET parameter, ΔG_1 , fitted for carbon segregation at $0.6T_m$. Recall that ΔG_1 represents the binding free energy for “innermost monolayer” of binding sites. As shown in the figure, standard measures of grain boundary configuration such as Σ value [panel (c)] and energy [panel (d)] correlate very poorly with ΔG_1 . The average grain boundary hydrostatic stress also correlates extremely weakly with ΔG_1 [panel (b)]. On the other hand, the average compressive hydrostatic stress is found to correlate very well with ΔG_1 [panel (a)], exhibiting a high coefficient of determination, $R^2 = 0.95$.

The strong correlation between compressive stress and ΔG_1 for carbon at $0.6T_m$ shown in Figure 6(a) may be

qualitatively understood in terms of the stress relief provided by the smaller substitutional carbon atom, an effect that has been previously demonstrated in simulations of defect-grain boundary interactions in mc-Si.^{45,84} However, it is notable that this stress relief effect can be fully captured with a single thermodynamic parameter over a wide range of grain boundary structures. It is also instructive to consider how the microscopic configuration of the various grain boundaries plays a role in setting this relationship. Three groupings of the various grain boundaries considered in this paper may be identified: (1) twin boundaries, (2) dislocation arrays, and (3) the high-energy, twist grain boundary. First, it is straightforward to observe that the segregation tendency increases with twinning order from -0.45 eV at the $\Sigma 3\{111\}$ to -0.68 eV at the $\Sigma 9\{221\}$ and to -0.84 eV at the $\Sigma 27\{552\}$ twin boundaries. Here, the segregation strength increases in accord with the increasing number of highly compressive sites as the twinning order increases. No impact is apparent from the concomitant increase in strongly tensile sites, which can be readily explained by the fact that these sites do not contribute to the segregation behavior.

Next, the group of $\langle 001 \rangle$ -tilt grain boundaries, which may be interpreted as dislocation arrays, exhibit ΔG_1 values that increase with increasing separation of the dislocation cores because closely spaced dislocation cores lead to some stress cancellation (see Figure 1). In particular, the $\Sigma 5\{310\}$ grain boundary has an average compressive stress that is approximately 30% of that for the $\Sigma 25\{430\}$ boundary (0.55 vs. 1.45 GPa). In fact, the $\Sigma 25\{430\}$ grain boundary exhibits the largest ΔG_1 for carbon segregation, supporting the notion that impurity segregation in mc-Si is often found to be very pronounced (1) at small-angle grain boundaries and (2) in crystal regions of high dislocation densities.^{4,85}

Finally, the single twist $\Sigma 5\{001\}$ grain boundary, with an energy density twice as large as the average energy of the other boundaries, is representative of the high-energy “random” grain boundaries that characterize the high-performance mc-Si

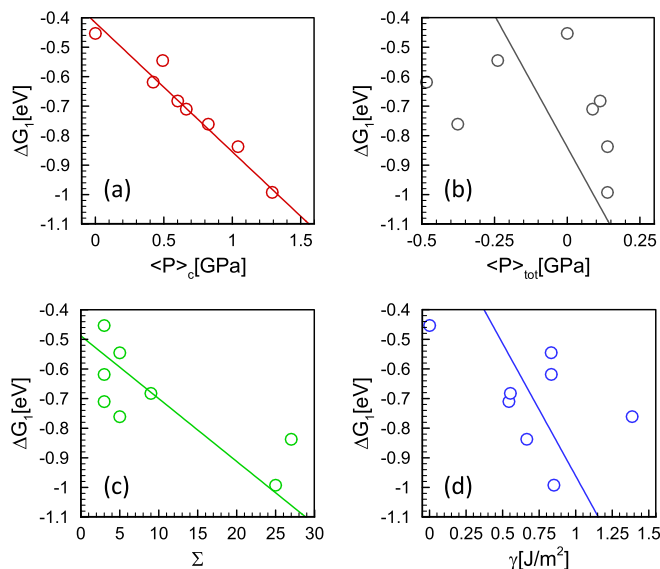


FIG. 6. Linear correlation between ΔG_1 and different measures of grain boundary structure for carbon segregation at $0.6T_m$. The R^2 values for the linear fits are (a) 0.95, (b) 0.14, (c) 0.63, and (d) 0.23.

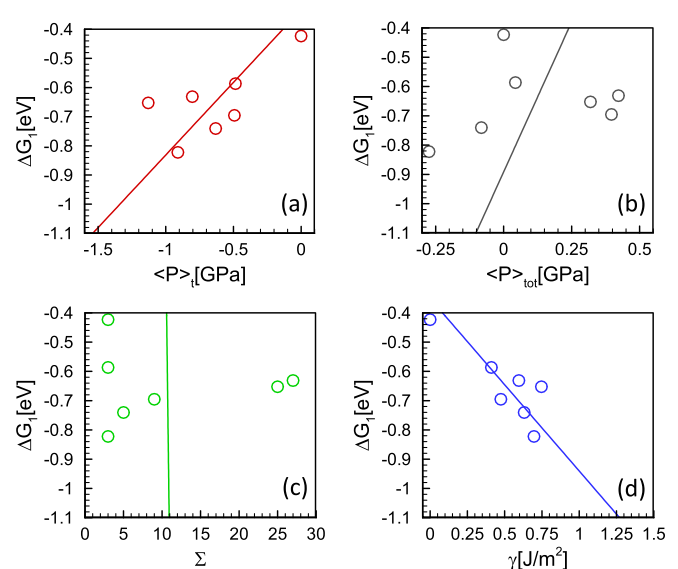


FIG. 7. Linear correlation between ΔG_1 and different measures of grain boundary structure for oxygen segregation at $0.6T_m$. The R^2 values for the linear fits are (a) 0.49, (b) 0.05, (c) 0.00, and (d) 0.72.

TABLE IV. Comparison of grain boundary energies (in J/m²) for the EA and the MT potentials.

GB type	$\Sigma 27 \{552\}$	$\Sigma 3 \{110\} / \{114\}$	$\Sigma 3 \{111\}$	$\Sigma 25 \{430\}$	$\Sigma 9 \{221\}$	$\Sigma 3 \{112\}$	$\Sigma 5 \{310\}$	$\Sigma 5 \{001\}$
γ -EA	0.665	0.543	0.000	0.851	0.553	0.833	0.832	1.386
γ -MT	0.596	0.411	0.000	0.746	0.475	0.697	0.631	1.206

discussed in the Introduction. Interestingly, the finite-capacity BET parameters for this structure show that, while the ΔG_1 value for the $\Sigma 5\{001\}$ grain boundary is rather average (-0.76 eV), the regressed values for the monolayer storage capacity ($X_{GB}^{ml} = 0.069$) and the number of monolayers ($n = 30$) is much higher than for the other grain boundaries. In other words, while isolated dislocation cores (as roughly represented by the $\Sigma 25$) attract a lot more carbon atoms in the dilute limit than a random, high-energy grain boundary (as represented by the $\Sigma 5\{001\}$), the latter is able to accumulate more carbon in the same grain boundary volume.

Not surprisingly, the picture for interstitial oxygen segregation, summarized in Figure 7, is somewhat different and also more difficult to characterize. Here, the best correlation for ΔG_1 is with the grain boundary energy ($R^2 = 0.72$), followed by the average tensile stress ($R^2 = 0.49$), although both are weaker than the best case for carbon. No correlation exists between ΔG_1 and the Σ value ($R^2 = 0.00$) or the total average stress ($R^2 = 0.05$). It is worth noting that the grain boundary energies are somewhat dependent on the potential (see Table IV) and may therefore confound the correlation to this quantity.

The correlation between interstitial oxygen segregation and average tensile stress also may be considered in the context of recent experimental results that show strong oxygen segregation at a highly tensile $\Sigma 9\{114\}$ grain boundary in silicon.⁸⁶ Moreover, Ohno⁸⁷ also find that oxygen segregation to small-angle tilt boundaries (consisting of arrays of edge dislocations) is strongly correlated with atomic sites that exhibit tensile hydrostatic stress above a threshold magnitude of about 2 GPa. Such findings will be useful for finding additional grain boundary measures that exhibit better correlation with the segregation model parameters.

Similar analyses for other parameters of the finite-capacity BET segregation model were attempted. Overall, the monolayer impurity fraction, X_{GB}^{ml} , which may be thought of as a monolayer “storage capacity,” was tested against various measures related to the stress distribution in a grain boundary. Generally, it was found that X_{GB}^{ml} for carbon at $0.6T_m$ correlates negatively with the number of low-stress ($|P| \leq 2$ GPa) sites. This “threshold” stress value is conceptually similar to the one proposed in Ref. 87 for oxygen segregation. Notably, there does not appear to be a strong positive correlation between X_{GB}^{ml} and the number of high-

stress sites ($|P| > 2$ GPa), suggesting that the distribution of high-binding sites amongst repulsive sites is important in establishing X_{GB}^{ml} . For interstitial oxygen segregation, correlations of X_{GB}^{ml} with measures of grain boundary structure are generally poor, and as noted earlier, are subject to a possible error due to the simplification of the interstitial configuration at high X_{BULK} . Another possible difficulty is that a single X_{GB}^{ml} parameter may be inadequate for making direct connections to grain boundary structure. Overall, these observations suggest that a more systematic search for appropriate coarse measures of grain boundary structure is required; future studies may benefit from recent developments in model reduction methods and data mining techniques.^{88,89}

VI. TEMPERATURE DEPENDENCE OF SEGREGATION

Impurity segregation at grain boundaries, like adsorption at surfaces and interfaces in general, may be influenced by entropic contributions that induce additional temperature dependence. Here, we interpret the temperature-dependence of carbon and oxygen segregation by calculating segregation

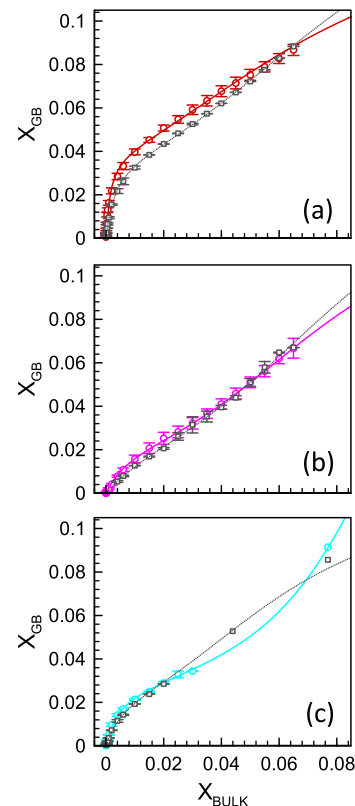


FIG. 8. Comparison of segregation isotherms at different temperatures [colored solid lines and circles $-0.6T_m$, grey dotted lines and squares $-0.8T_m$]. Symbols represent computational data and lines represent best fit cases of the BET model. (a) carbon@ $\Sigma 27\{552\}$; (b) carbon@ $\Sigma 3\{112\}$; (c) oxygen@ $\Sigma 9\{221\}$.

TABLE V. Vibrational entropies for carbon segregation.

Grain boundary type	$S_{vib,1}$ (meV/K)	$S_{vib,L}$ (meV/K)
$\Sigma 27\{552\}$	0.30	0.18
$\Sigma 9\{221\}$	0.26	0.18
$\Sigma 3\{112\}$	0.12	0.18

vibrational entropies for the two BET “layers,” $S_{vib,1}$ and $S_{vib,L}$, from the temperature dependence of the regressed ΔG_1 and ΔG_L values for carbon segregation at selected grain boundaries; see Table V. Similar trends and values are obtained for oxygen (data not shown). The effect of temperature on the segregation isotherms for carbon and oxygen at $0.6T_m$ and $0.8T_m$ is shown explicitly in Figure 8 (corresponding model parameters were provided in Table II). Interestingly, the values for S_{vib} are in good quantitative agreement with the experimental study in Ref. 83 where tin segregation in iron lead a vibrational entropy of 0.28 meV/K.

VII. CONCLUSIONS

The segregation of impurity atoms to grain boundaries and dislocations remains a key factor in establishing the quality of multicrystalline silicon. Although experimental techniques have now evolved to the point of providing very detailed views of impurity atom distributions, atomistic simulations provide a relatively facile, complementary approach for studying segregation, and in particular, for probing mechanistic subtleties that are otherwise difficult to access.

In this paper, we used a compound approach to probe the relationships between grain boundary descriptors and segregation behavior. We first performed a detailed atomistic investigation of carbon and oxygen segregation to various types of grain boundaries in silicon using quasi-on lattice Grand Canonical Monte Carlo simulations to compute segregation isotherms across a wide range of loading conditions and at two different temperatures. While direct atomistic calculations of segregation provide a highly detailed view of segregation as a function of impurity atom loading and other variables, native descriptions of grain boundary structure (atomic configurations) and segregation behavior (segregation strength at each impurity loading extent and temperature) are both “high-dimensional,” making it difficult to establish mechanistically meaningful connections between segregation behavior and grain boundary properties. We facilitated this task by regressing the segregation data to simplified analytical models based on a few, physically transparent parameters. It was found that a four-parameter, multilayer model (the finite BET isotherm) was necessary, and apparently sufficient, to capture the segregation behavior of carbon and oxygen for all conditions considered in the present work.

The regressed BET parameters were then correlated with various grain boundary measures. It was found that measures related to the distribution of atomic stresses were most likely to provide quantitative correlation with the segregation isotherm parameters. In particular, the carbon segregation free energy within the first monolayer (ΔG_1) was found to correlate extremely well with the average hydrostatic pressure of all compressive sites in a grain boundary—the correlation was much weaker if all sites (i.e., including tensilely stressed ones) were included. Recent experimental findings also support the notion that only certain sub-populations of atoms should be considered when establishing correlations between grain boundary properties and segregation behavior. While reasonably good

correlations also were found between ΔG_1 and better-established grain boundary properties such as sigma-value and energy, in agreement with numerous previous experimental and theoretical studies, these correlations tended to be somewhat qualitative in nature and exhibit a significant amount of scatter about the line of best-fit. In other words, quantities like the energy density are likely to be too coarse to account properly for all grain boundary nuances that impact ΔG_1 . Consequently, while an overall trend may be identified with respect to properties such as energy density, these correlations generally cannot be used to make quantitative predictions.

In contrast to the carbon case, the oxygen segregation results presented here should be regarded as preliminary and are certainly expected to be less conclusive than the corresponding carbon segregation results. The primary challenge associated with computing segregation isotherms for oxygen lies in the interstitial nature of atomic oxygen in silicon. While the potential model employed in this paper appears to describe well the configuration of the single oxygen interstitial, it is very difficult to identify the relaxed configurations that correspond to multiple oxygen atoms without global searches that require lengthy molecular simulations at finite temperature. By contrast, the local energy minimization technique utilized in this work assumes initially that all oxygen atoms lie on similar interstitial sites even when in close proximity (e.g., under high loading), and that only “downhill” searches are needed to find the relaxed configurations. These strong assumptions notwithstanding, the present approach should provide a reasonable representation of oxygen segregation at low-to-moderate loading, where oxygen-oxygen atom interactions are weak. The fact that correlations between the regressed BET isotherm parameters and various grain boundary measures were less apparent than for the corresponding carbon cases is likely to be a direct result of the interstitial nature of oxygen. Consequently, it may be the measures that incorporate information beyond hydrostatic pressure at each atomic site will be needed to generate correlations that are quantitative enough for prediction. Such complex measures are not likely to be found with a trial-and-error approach and instead will require the use of automated data-mining techniques.

Overall, while certainly not comprehensive, the present work suggests a viable pathway for systematically generating property/segregation relationships for various impurities on grain boundaries in multicrystalline silicon. Such relationships would provide a powerful diagnostic tool for optimizing multicrystalline silicon, especially as more capability is gained for grain boundary distribution control.

ACKNOWLEDGMENTS

This work was partly supported by the German Federal Ministry for the Environment, Nature Conservation and Nuclear Safety via research cluster SolarWinS (0327259 B) projects and the industry partners. The content of this publication is the responsibility of the authors. We would also like to thank Professor Michael Seibt for support and numerous helpful discussions related to this work.

- ¹B. Wu, N. Stoddard, R. Ma, and R. Clark, *J. Cryst. Growth* **310**, 2178 (2008).
- ²T. F. Li, K. M. Yeh, W. C. Hsu, and C. W. Lan, *J. Cryst. Growth* **318**, 219 (2011).
- ³C. W. Lan, W. C. Lan, T. F. Lee, A. Yu, Y. M. Yang, W. C. Hsu, B. Hsu, and A. Yang, *J. Cryst. Growth* **360**, 68 (2012).
- ⁴G. Sarau, S. Christiansen, M. Holla, and W. Seifert, *Sol. Energy Mater. Sol. Cells* **95**, 2264 (2011).
- ⁵K. Fujiwara, W. Pan, K. Sawada, M. Tokairin, N. Usami, Y. Nose, A. Nomura, T. Shishido, and K. Nakajima, *J. Cryst. Growth* **292**, 282 (2006).
- ⁶K. Fujiwara, W. Pan, N. Usami, K. Sawada, M. Tokairin, Y. Nose, A. Nomura, T. Shishido, and K. Nakajima, *Acta Mater.* **54**, 3191 (2006).
- ⁷X. Gu, X. Yu, K. Guo, L. Chen, D. Wang, and D. Yang, *Sol. Energy Mater. Sol. Cells* **101**, 95 (2012).
- ⁸Y. Yang, A. Yu, B. Hsu, W. Hsu, A. Yang, and C. Lan, *Prog. Photovoltaics: Res. Appl.* **23**, 340 (2015).
- ⁹H. J. Möller, T. Kaden, S. Scholz, and S. Wuerzner, *Appl. Phys. A* **96**, 207 (2009).
- ¹⁰M. Seibt, V. Kveder, W. Schröter, and O. Voß, *Phys. Status Solidi A* **202**, 911 (2005).
- ¹¹M. Seibt, D. Abdelbarey, V. Kveder, C. Rudolf, P. Saring, L. Stolze, and O. Voss, *Mater. Sci. Eng., B* **159–160**, 264 (2009).
- ¹²S. Scholz, PhD thesis, “Kohlenstoff in EFG-Silizium: Verteilung und Einfluss auf die Rekombinationseigenschaften,” Technical University Bergakademie Freiberg, 2008.
- ¹³M. Seibt, R. Khalil, V. Kveder, and W. Schröter, *Appl. Phys. A* **96**, 235 (2009).
- ¹⁴J. Rakotoniaina, O. Breitenstein, M. Werner, M. H. Al-Rifai, T. Buonassisi, M. Pickett, M. Ghosh, A. Müller, and N. Le Quang, Proceedings of the 20th EU PVSEC, Barcelona, Spain, 2005.
- ¹⁵O. Breitenstein, J. Bauer, and J. P. Rakotoniaina, *Semiconductors* **41**, 440 (2007).
- ¹⁶L. Liu, S. Nakano, and K. Kakimoto, *J. Cryst. Growth* **310**, 2192 (2008).
- ¹⁷P. Lejcek and S. Hofmann, *Crit. Rev. Solid State Mater. Sci.* **20**, 1 (1995).
- ¹⁸W. Thomas and B. Chalmers, *Acta Metall. Mater.* **3**, 17 (1955).
- ¹⁹T. Watanabe, S. Kitamura, and S. Karashima, *Acta Metall. Mater.* **28**, 455 (1980).
- ²⁰T. Watanabe, T. Murakami, and S. Karashima, *Scr. Metall. Mater.* **12**, 361 (1978).
- ²¹K. Tatsumi, N. Okumura, and S. Funaki, *Trans. Jpn. Inst. Met.* **27**, 427 (1985).
- ²²S. Hofmann, P. Lejcek, and J. Adámek, *Surf. Interface Anal.* **19**, 601 (1992).
- ²³S. Suzuki, K. Abiko, and H. Kimura, *Scr. Metall. Mater.* **15**, 1139 (1981).
- ²⁴P. Lejcek and S. Hofmann, *Surf. Interface Anal.* **16**, 546 (1990).
- ²⁵P. Lejcek, *Anal. Chim. Acta* **297**, 165 (1994).
- ²⁶P. Lejcek, J. Adámek, and S. Hofmann, *Surf. Sci.* **264**, 449 (1992).
- ²⁷T. Buonassisi *et al.*, *Prog. Photovoltaics: Res. Appl.* **14**, 513 (2006).
- ²⁸T. Buonassisi, A. A. Istratov, M. D. Pickett, M. A. Marcus, T. F. Ciszek, and E. R. Weber, *Appl. Phys. Lett.* **89**, 042102 (2006).
- ²⁹B. Chen, J. Chen, T. Sekiguchi, M. Saito, and K. Kimoto, *J. Appl. Phys.* **105**, 113502 (2009).
- ³⁰M. Chisholm, A. Maiti, S. Pennycook, and S. Pantelides, *Phys. Rev. Lett.* **81**, 132 (1998).
- ³¹C. Wong, C. R. Grovenor, P. Batson, and D. Smith, *J. Appl. Phys.* **57**, 438 (1985).
- ³²A. Carabelas, D. Nobili, and S. Solmi, *J. Phys.-Paris* **43**, C1-187 (1982).
- ³³M. M. Mandurah, K. C. Saraswat, C. R. Helms, and T. I. Kamins, *J. Appl. Phys.* **51**, 5755 (1980).
- ³⁴J. Rose and R. Gronsky, *Appl. Phys. Lett.* **41**, 993 (1982).
- ³⁵A. Stoffers, O. Cojocar-Mirédin, W. Seifert, S. Zaefferer, S. Riepe, and D. Raabe, “Grain boundary segregation in multicrystalline silicon: correlative characterization by EBSD, EBIC, and atom probe tomography,” *Prog. Photovoltaics: Res. Appl.* (published online).
- ³⁶D. Duffy and P. Tasker, *Philos. Mag. A* **50**, 155 (1985).
- ³⁷S. Benlamari, N. H. Djaballah, D. E. Mekki, and C. J. Monty, *Mater. Sci. Eng., C* **26**, 169 (2006).
- ³⁸S. M. Foiles, *Phys. Rev. B* **40**, 11502 (1989).
- ³⁹M. Menyhard, M. Yan, and V. Vitek, *Acta Metall. Mater.* **42**, 2783 (1994).
- ⁴⁰H. Wang, R. Najafabadi, D. Srolovitz, and R. LeSar, *Philos. Mag. A* **65**, 625 (1992).
- ⁴¹D. Udler and D. Seidman, *Acta Metall. Mater.* **42**, 1959 (1994).
- ⁴²A. Seki, D. Seidman, Y. Oh, and S. Foiles, *Acta Metall. Mater.* **39**, 3167 (1991).
- ⁴³O. H. Duparc, A. Larere, B. Lezzar, O. Khalfallah, and V. Paidar, *J. Mater. Sci.* **40**, 3169 (2005).
- ⁴⁴K. Masuda-Jindo and Y. Fujita, *Solid State Phenom.* **51–52**, 27 (1996).
- ⁴⁵P. Kāshammer and T. Sinno, *J. Appl. Phys.* **114**, 083505 (2013).
- ⁴⁶S. Munetoh, T. Motooka, K. Moriguchi, and A. Shintani, *Comp. Mater. Sci.* **39**, 334 (2007).
- ⁴⁷T. Watanabe, D. Yamasaki, K. Tatsumura, and I. Ohdomari, *Appl. Surf. Sci.* **234**, 207 (2004).
- ⁴⁸J. G. Yu, S. B. Sinnott, and S. R. Phillpot, *Phys. Rev. B* **75**, 085311 (2007).
- ⁴⁹J. Tersoff, *Phys. Rev. B* **39**, 5566 (1989).
- ⁵⁰R. Devanathan, T. D. de la Rubia, and W. J. Weber, *J. Nucl. Mater.* **253**, 47 (1998).
- ⁵¹P. Erhart and K. Albe, *Phys. Rev. B* **71**, 035211 (2005).
- ⁵²J. Pohl, M. Mueller, A. Seidl, and K. Albe, *J. Cryst. Growth* **312**, 1411 (2010).
- ⁵³C. Y. Chuang, Q. M. Li, D. Leonhardt, S. M. Han, and T. Sinno, *Surf. Sci.* **609**, 221 (2013).
- ⁵⁴M. Pesola, J. Von Boehm, T. Mattila, and R. Nieminen, *Phys. Rev. B* **60**, 11449 (1999).
- ⁵⁵K. A. Jackson, *Handbook of Semiconductor Technology* (Wiley, 2000), Vol. 1, p. 379.
- ⁵⁶M. A. Tschoop and D. L. McDowell, *Philos. Mag.* **87**, 3147 (2007).
- ⁵⁷J. Zhang, C. Z. Wang, and K. M. Ho, *Phys. Rev. B* **80**, 174102 (2009).
- ⁵⁸M. D. Vaudin, B. Cunningham, and D. G. Ast, *Scr. Metall. Mater.* **17**, 191 (1983).
- ⁵⁹D. P. Divincenzo, O. L. Alerhand, M. Schluter, and J. W. Wilkins, *Phys. Rev. Lett.* **56**, 1925 (1986).
- ⁶⁰N. Sakaguchi, H. Ichinose, and S. Watanabe, *Mater. Trans.* **48**, 2585 (2007).
- ⁶¹M. Kohyama and K. Tanaka, *Mater. Sci. Forum* **294–296**, 231 (1999).
- ⁶²M. Kohyama and R. Yamamoto, *Phys. Rev. B* **49**, 17102 (1994).
- ⁶³F. Cleri, *Comp. Mater. Sci.* **20**, 351 (2001).
- ⁶⁴S. Plimpton, *J. Comput. Phys.* **117**, 1 (1995).
- ⁶⁵A. Stukowski, *Modell. Simul. Mater. Sci.* **18**, 015012 (2010).
- ⁶⁶A. E. Mora, J. W. Steeds, and J. E. Butler, *Diamond Relat. Mater.* **11**, 697 (2002).
- ⁶⁷A. Voigt, E. Wolf, and H. P. Strunk, *Mater. Sci. Eng., B* **54**, 202 (1998).
- ⁶⁸B. Gallien, T. Duffar, S. Lay, and F. Robaut, *J. Cryst. Growth* **318**, 208 (2011).
- ⁶⁹S. Foiles, *Phys. Rev. B* **32**, 7685 (1985).
- ⁷⁰D. Frenkel and B. Smit, *Understanding Molecular Simulation: From Algorithms to Applications* (Academic Press, 2001), Vol. 1.
- ⁷¹H. A. Murdoch and C. A. Schuh, *J. Mater. Res.* **28**, 2154 (2013).
- ⁷²P. Wynblatt and D. Chatain, *Metall. Mater. Trans. A* **37**, 2595 (2006).
- ⁷³I. Langmuir, *J. Am. Chem. Soc.* **38**, 2221 (1916).
- ⁷⁴S. Brunauer, P. H. Emmett, and E. Teller, *J. Am. Chem. Soc.* **60**, 309 (1938).
- ⁷⁵C. L. White and W. A. Coghlan, *Metall. Trans. A* **8**, 1403 (1977).
- ⁷⁶D. McLean, *Grain Boundaries in Metals* (Clarendon Press, 1957).
- ⁷⁷R. Fowler and E. Guggenheim, *Statistical Thermodynamics* (Cambridge University Press, 1939).
- ⁷⁸T. Chookajorn and C. A. Schuh, *Phys. Rev. B* **89**, 064102 (2014).
- ⁷⁹P. Wynblatt and R. Ku, *Surf. Sci.* **65**, 511 (1977).
- ⁸⁰Y. Lee and H. Aaronson, *Surf. Sci.* **95**, 227 (1980).
- ⁸¹Y. Lee and H. Aaronson, *Acta Metall. Mater.* **28**, 539 (1980).
- ⁸²M. Seah and E. Hondros, *Proc. R. Soc. London, Ser. A* **335**, 191 (1973).
- ⁸³M. Seah, *J. Phys. F: Met. Phys.* **10**, 1043 (1980).
- ⁸⁴K. Masuda-Jindo, *Diffus. Defect Data, Pt. B* **37–38**, 125 (1994).
- ⁸⁵S. Pizzini, A. Sandrinelli, M. Beghi, D. Narducci, and P. L. Fabbri, *Rev. Phys. Appl.* **22**, 631 (1987).
- ⁸⁶Y. Ohno, private communication (2015).
- ⁸⁷Y. Ohno, private communication (2015).
- ⁸⁸A. L. Ferguson, A. Z. Panagiotopoulos, I. G. Kevrekidis, and P. G. Debenedetti, *Chem. Phys. Lett.* **509**, 1 (2011).
- ⁸⁹B. Nadler, S. Lafon, R. R. Coifman, and I. G. Kevrekidis, *Appl. Comput. Harmon. Anal.* **21**, 113 (2006).